Journal of Membrane Science 595 (2020) 117477

Contents lists available at ScienceDirect

Journal of Membrane Science

journal homepage: www.elsevier.com/locate/memsci

Phase inversion/sintering-induced porous ceramic microsheet membranes for high-quality separation of oily wastewater

Liang Yu, Masakoto Kanezashi, Hiroki Nagasawa, Toshinori Tsuru*

Department of Chemical Engineering, Hiroshima University, 1-4-1 Kagamiyama Higashihiroshima, 739-8527, Japan

ARTICLE INFO

Keywords:
Ceramic microsheets
Phase inversion
Superhydrophilicity
Underwater superoleophobicity
Oily wastewater treatment

ABSTRACT

Ceramic microfiltration membranes with superior chemical and mechanical stability for sustainable operation under harsh conditions have demonstrated great potential for industrial wastewater treatment. In this study, low-cost ceramic microsheet membranes with a thickness of sub-0.5 mm that possess superhydrophilic and underwater superoleophobic properties were fabricated from an Al_2O_3-rich Al_2O_3/polysulfone composite slurry via a phase inversion/sintering strategy. The cross-sectional morphologies of these phase inversion-induced composite films appear as ceramic green bodies that can be precisely controlled by tuning the operation parameters during the classic phase-inversion process of a polymer, which allows the morphology to withstand a subsequent high-temperature (1250 °C) sintering process. The thinner nature (< 0.5 mm), suitable pore size ($\sim$100 nm), and a superior wetting chemistry make these ceramic microsheets very promising for the separation of oil-in-water emulsions with an outstanding separation efficiency of $> 99\%$ and a much higher emulsion permeability of $\sim$3,000 L/(m^2 h bar), which is 2 orders of magnitude higher than most commercially available microfiltration membranes that are capable of similar levels of separation performance. This process resulted in a favorable membrane that combines robustness under complex chemical environments with low cost for both materials and processing approaches, which should facilitate its practical application in the industrial treatment of oily wastewater.

1. Introduction

Oily wastewater is generated in many industries and oil spill accidents, which has become a serious global environmental concern [1]. The oil and gas industry, for instance, produces approximately 14 billion barrels (2.2×10^{10} m^3) of water annually, and this so-called produced water is made up largely of salts and oil hydrocarbons, which can differ widely from well to well [2]. The oil phase in wastewater generally presents at least three forms that are classified based on the size of oil droplets: free oil (> 150 μm), dispersed oil (20–150 μm), and emulsified oil (< 20 μm) [3]. The diversity and complexity of the oily wastewater, particularly oil-in-water emulsions with micron (20 μm) and nano-scale (< 100 nm) oil droplets, makes separation a daunting challenge via conventional techniques such as settling tanks, centrifugation, the use of skimmers, air flotation, and biological degradation [4]. Therefore, membrane-based technologies have attracted great attention for the separation of oil/water mixtures because they are energy-efficient, cost-effective and applicable to a wide range of oily wastewater [1,5,6]. Functionalized mesh membranes have recently been extensively studied because of their simplicity and gravity-driven high flow rates [7–13]. These meshes have a large pore structure and a super-wetting surface chemistry that demonstrates superior separation performance for laboratory-scale oil/water mixtures, but there are limitations for the practical use of separation of emulsified oil/water mixtures [14,15]. In addition, only several commercially available membranes have been designed and marketed for oily industrial wastewater treatment, as listed in Table 1 [6]. Most of them, however, are polymeric ultrafiltration (UF) membranes (pore size, $\sim$2–50 nm) that exhibit a relatively lower level of permeation flux. Consequently, the development of cost-effective, advanced filtration membranes for the highly efficient separation of oil/water mixtures with a high flow rate and robustness under various conditions is greatly desired. This intention requires strict consideration for both the pore structure (e.g., size and distribution, density, and length) and the surface wettability along with a design that will balance separation efficiency and permeation flux.

Thus far, two types of membranes have been designed and fabricated based on surface wettability: oil removing and water removing. The oil-removing membranes have a superhydrophobic/superoleophilic surface wettability that the oil phase can selectively permeate. On the

---

* Corresponding author.
E-mail address: tsuru@hiroshima-u.ac.jp (T. Tsuru).

https://doi.org/10.1016/j.memsci.2019.117477
Received 27 June 2019; Received in revised form 10 September 2019; Accepted 16 September 2019

Table 1
Commercially available membranes designed for industrial oily wastewater treatment.

Manufacture	Membrane material	Filtration type	Pore size [nm]	Configuration
Osmonics	Chemically modified PAN	Ultrafiltration	10	Spiral wound
Filtration Solution Inc.	Chemically modified PAN	Ultrafiltration	10	Spiral wound
Hydranautics	Composite polyamide	Reverse osmosis	–	Spiral wound
Clean Water Technologies	Hydrophilic PAN	Ultrafiltration	10–100	Hollow Fiber
Veolia Water Technologies	TiO_2	Ultrafiltration	100	Tubular

contrary, the water-removing membranes have superhydrophilic/superoleophobic surfaces that allow permeation of the water phase. However, these oil-removing membranes usually encounter two key disadvantages: (i) the membrane surface is more easily fouled by the oils due to an intrinsic oleophilic nature; and, (ii) most oils such as light hydrocarbons have a lower density than water, which can form a barrier between the oil phase and the membrane surface. Furthermore, in many oil fields, more water is emitted than oil, which results in the formation of water-rich oily wastewater [16]. Consequently, water-removing membranes are more attractive for attempts to reduce membrane fouling by oils and to meet the requirements of most practical applications in an energy-efficient manner. Unlike polymeric membranes, the use of oxide ceramic membranes that are generally superhydrophilic, provides several benefits that include sufficient mechanical and thermal stability, high solvent resistance, and ease of cleaning and washing by strong acidic and alkaline solutions to address the membrane fouling issues. Membrane fouling, as a result of the cumulative deposition of constituents like oil on the membrane surface and inside the pores leads to a significant decline in the permeate flux, and is the key drawback that limits the broader implementation of membrane-based oil/water separations [3].

Typically, oxide ceramic membranes such as Al_2O_3, SiO_2, ZrO_2, TiO_2, and their composites have an asymmetric multi-layered structure with a macroporous ceramic support and several subsequently generated intermediate layers for gradually minimizing the pore sizes. Accordingly, the fabrication of such oxide ceramic membranes requires multiple coating-sintering processes, which is both energy-intensive and time-consuming and in turn too expensive for industrial oily wastewater treatment [17]. Therefore, a reduction in the cost of oxide ceramic membranes would be significant in order to improve competitiveness in practical applications. The early development of ceramic membranes via phase inversion/sintering was reported by Luyten et al. [18] for the fabrication of LaSrCoFeO3-x membranes. Unlike the preparation of polymeric membranes via phase inversion, this approach used a ceramic-dominant mixture with appropriate ceramic powders as the major component and the polymer as a binder. During the subsequent sintering process, the polymer was burned off, which generated porosity. By using the phase inversion/sintering method, the asymmetric ceramic membranes can be obtained in a single step, which can significantly reduce cost. Generally, this method is used to produce hollow fiber ceramic membranes with a high surface/volume ratio and enhanced mechanical strength [19–22]. Investigations of ceramic membranes with flat-sheet configurations, particularly those with finger-like structure, have so far been very limited.

Based on the Hagen-Poiseuille equation, which is generally used to describe the classical dynamic theory, the permeation flux of UF/MF membranes is directly proportional to the surface porosity and square of the effective pore size, and inversely proportional to the membrane thickness. This implies that an ideal filtration membrane for oil/water separation should demonstrate higher surface porosity, lower active membrane thickness, and a suitable pore size. Considering the complexity of oily wastewater (pH, oil droplet size, etc.), ultrathin, high-porosity oxide ceramic membranes are therefore preferred for the practical treatment of oily wastewater.

Herein, we report the fabrication of low-cost, high-porosity, ceramic-microsheet membranes with a thickness of sub-0.5 mm via phase inversion/sintering using Al_2O_3 particles (~0.2 µm) as the ceramic materials and polysulfone (PSf) as either the binder or microstructure-directing agent. Ceramic green bodies with different cross-sectional morphologies can be fabricated by tuning the parameters of the phase inversion process. The morphology evolution of the achieved ceramic microsheets was studied. Uniform-pressure compression was used to evaluate the mechanical strength of these ceramic microsheets. Both liquid- and gas-permeation tests were conducted to assess the microsheet membrane performance. Most importantly, these ceramic microsheets could be successfully applied to the separation of emulsified oil/water mixtures with outstanding stable permeation flux and oil-removal efficiency.

2. Experimental

2.1. Fabrication of ceramic microsheets

A mass composition of Polysulfone/Pluronic F-127/Al_2O_3 powders/N-Methylpyrrolidone = 1/0.2/5/7 was used to prepare a ceramic suspension with appropriate viscosity that could form composite films with good quality. Polysulfone (PSf, M_n = 22,000, SIGMA-ALDRICH, US) and Pluronic F-127 (F-127, M_n = 12,600, SIGMA-ALDRICH, US) were dissolved in N-Methylpyrrolidone (NMP, SIGMA-ALDRICH, US) by magnetic stirring at 60 °C for 24 h to form a homogenous solution, prior to the addition of Al_2O_3 powders (~0.2 µm, AKP-50, SUMITOMO CHEMICAL Co., LTD, Japan). To improve the dispersion of Al_2O_3 powders, the ceramic suspension with high viscosity was then ball-milled using high density ceramic balls (diameter, 1 mm) for 48 h at ambient temperature, followed by ultrasonic treatment for 0.5 h and settling for 6 h to remove air bubbles. Thanks to the use of a dispersion agent (Pluronic F-127) and the smaller size of Al_2O_3 particles, no obvious settled powders were observed in the ceramic suspension after settling.

The degassed ceramic suspension was poured onto a clean, smooth glass plate and cast using a thickness-controllable doctor blade (Scheme 1). The cast film was immersed in either distilled water or pure ethanol

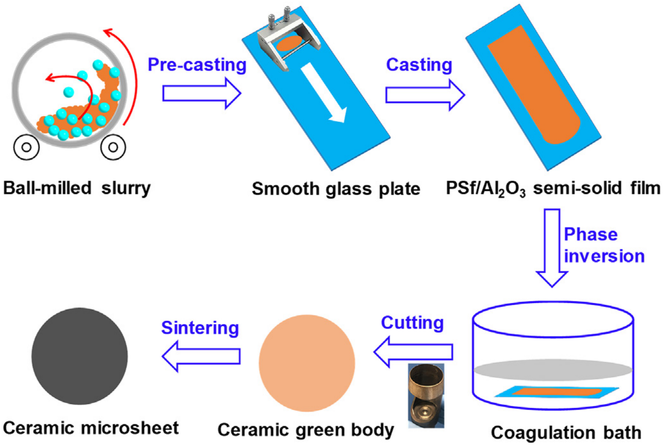

Scheme 1. Schematic diagram of the fabrication of ceramic microsheets via phase inversion/sintering.

immediately or after a certain hold-up duration at 50 °C in a drying oven to form a finger-like, sponge-like and dense structure, respectively. The solidified ceramic green bodies (PSf/Al_2O_3 solid films) could be separated from the glass plate automatically after 0.5 h. The detached films were then stored in distilled water or pure ethanol to allow complete phase inversion.

Before the sintering process, the ceramic green bodies were cut into circular pieces using a circular cutting knife (diameter, 28 mm). The circular green bodies were then sandwiched with smooth Al_2O_3 plates and subjected to a temperature-programed sintering process in a Muffle furnace (FP410, YAMATO, Japan) under an air atmosphere. Accordingly, the circular green bodies were heated at 150 °C for 0.5 h to remove the adsorbed solvent, and then at 600 °C for 2 h to burn off the organic polymers (PSf and F127). They then were sintered at 1,250 °C for 2 h to promote the formation of densely packed Al_2O_3 particles that were loosely packed in the green bodies. A heating rate of 3 °C/min was employed for each step. The achieved ceramic microsheets were denoted as AO-X-Y, where X represents the type of phase inversion media (W for water, E for ethanol, and A for solidification in air) and Y is the thickness of the final ceramic microsheets.

2.2. Preparation of oil-in-water emulsions

Surfactant-stabilized oil-in-water emulsions were prepared by mixing mineral oil with water in a volume ratio of 1:1,000 using a high-speed homogenizer (IKA® T18 digital ULTRA-TURRAX®, IKA GmbH, Germany) at room temperature. Sodium dodecyl sulfonate (SDS) aqueous solution (10 mL, 0.01 g/mL) was subsequently added to the oil/water mixture (1 L) as an emulsifier. The solution was emulsified with a speed of 20,000 rpm for 30 min to form an opaque emulsion. The oil droplet size was determined via dynamic light scattering (DLS) using a Malvern Zetasizer Nano ZS (Malvern Instruments, Ltd., UK) at 25 °C, and the oil content (ppm) in the water was quantitatively analyzed using an ultraviolet–visible (UV–vis) spectrophotometer (V-570, JASCO, Japan) based on the absorbance of oil-in-water emulsions at 231 nm. All the emulsions were allowed to stabilize for 24 h and were directly used for separation.

2.3. Characterizations of ceramic microsheets

The weight evolution with temperature of ceramic green bodies was probed via thermogravimetric mass spectrometer (TG-MS, TGA-DTA-PIMS 410/S, Rigaku, Japan). The thickness and diameter of the obtained ceramic microsheets was measured using a digital micrometer (Mituloyo, Japan). The surface and cross-sectional morphologies were observed using a JCM 5700 scanning electron microscope (SEM, JEOL, Japan).

The porosity of the ceramic microsheets was measured via a gravimetric method and was calculated using Eq. (1).

$$\varepsilon = \frac{(m_w - m_d)/\rho_w}{(m_w - m_d)/\rho_w + m_d/\rho_c} \times 100\% \tag{1}$$

In Eq. (1), ε is the porosity (%), m_w and m_d are the mass values (g) of the water-wetted and dried ceramic microsheets, respectively, and ρ_w and ρ_c are the densities of water (0.998 g/cm^3) and the ceramic powders (3.97 g/cm^3). Three samples for each ceramic microsheet were measured in parallel to establish the arithmetic mean.

The shrinking effect of the ceramic microsheets from ceramic green bodies was evaluated based on the shrinking ratios (θ, %) in both thickness and diameter using Eq. (2).

$$\theta = \left(1 - \frac{A_2}{A_1}\right) \times 100\% \tag{2}$$

In Eq. (2), A_1 and A_2 are the values of either thickness or diameter for the ceramic green bodies and the final ceramic microsheets, respectively.

The surface wettability of the microsheet membranes was examined by using a contact angle meter (DM300, Kyowa Interface Science, Japan) to measure both the water and oil contact angles in air and the underwater oil contact angle. To measure the contact angles in air, water or oil (mineral oil) droplets (0.2 μL) were directly dropped onto the membrane surface using a microsyringe. When measuring the underwater oil contact angles, the microsheet membranes were first fixed on a glass slide and then wetted by water. The glass slide was then placed into a self-designed system that included a transparent polycarbonate container that served as the water reservoir. Then, a 0.2 μL droplet of oil (tetrachloromethane) was carefully dropped onto the membrane surface. The contact angle of each sample was obtained by measuring three different positions, and the average value was then calculated. In addition, the underwater dynamic oil adhesion and underwater sliding behaviors of oil droplets were also investigated using tetrachloromethane as the detected oil.

To evaluate the membrane performance of these ceramic microsheets, both gas (N_2) and liquid (pure water) permeation tests were conducted in homemade apparatuses, as illustrated in Figures S6 (ESI-5) and S9 (ESI-6), respectively, at room temperature. A ceramic membrane with a diameter of ~25 mm was installed in a flat type of membrane module that contained a porous metal plate to support the microsheets and annular silicone rubber as sealing materials. The water and N_2 permeate flow rates under various transmembrane pressure drops were measured using a digital mass balance (AUW220D, SHIMADZU, Japan) and a soap film flow meter (HORIBASTEC, Japan), respectively. All the permeation tests were conducted at room temperature. The Hagen-Poiseuille equation was used to describe the water permeation behaviors of ceramic membranes, as shown in Eq. (3).

$$J = \frac{\varepsilon r_p^2 \Delta p}{8\mu l} \tag{3}$$

In Eq. (3), J is the permeation flux, ε is the surface porosity, r_p is the membrane pore radius, Δp is the transmembrane pressure drop, μ is the viscosity of the liquid, and l is the total distance that the liquid travels through the membrane.

A compression test of the ceramic microsheets was conducted using the same apparatus as that used in the gas permeation test where the porous metal support was removed and the microsheet samples were wetted by water, as depicted in Figures S7 and S8 (ESI-5). The critical stress (σ, kPa) from fracture can be calculated using Eq. (4).

$$\sigma = \frac{3\Delta p R^2}{4l^2} \tag{4}$$

In Eq. (4), Δp (kPa) is the critical pressure drop from a rupture applied to the microsheet by the feed-to-permeate process, and R (mm) and l (mm) are the installed radius and thickness of a circular sample, respectively.

2.4. Oil/water separation test

A cross-flow filtration apparatus (Figure S9, ESI-6) was employed to evaluate the oil/water emulsion separation capability of the ceramic microsheets. Prior to the oil/water separation, a gas permeation test of the water-wetted ceramic microsheets (the so-called bubble-point test) was conducted to verify their integrity. The water or emulsion flux (J, L/(m^2 h)) and permeability (P, L/(m^2 h bar)) in *trans*-membrane pressure ranges of 0.02–0.3 MPa were calculated using Eqs. (5) and (6).

$$J = \frac{V}{At} \tag{5}$$

$$P = \frac{V}{At\Delta p} = \frac{J}{\Delta p} \tag{6}$$

In Eqs. (5) and (6), V (L) is the volume of the permeate, A (m^2) is the

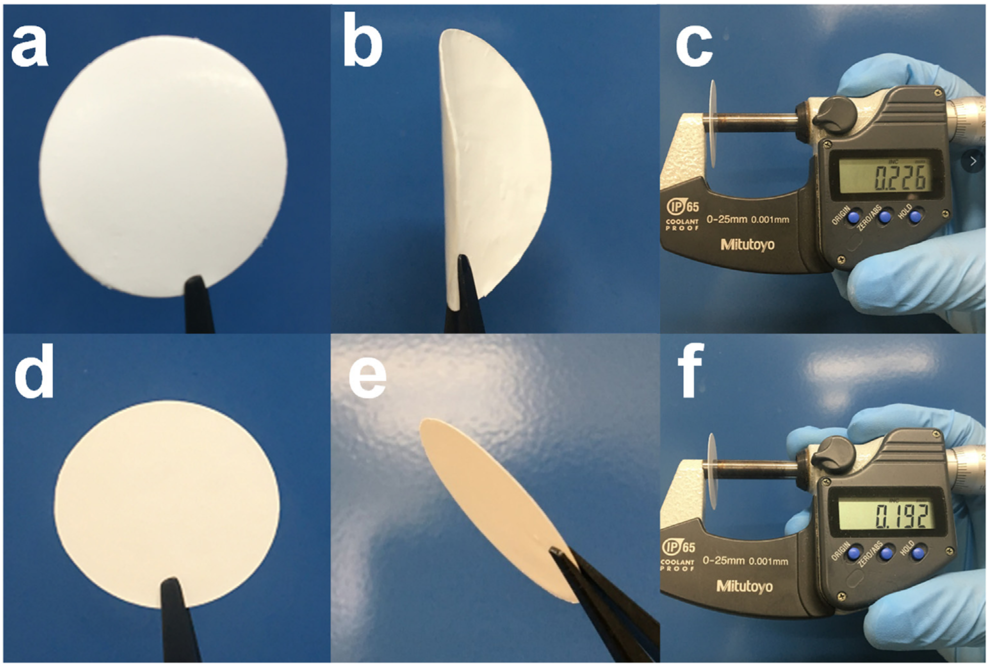

Fig. 1. Digital photos of (a–c) ceramic green bodies with smooth and flexible properties and (d–f) very thin ceramic microsheets.

effective filtration area of the membrane, and t (h) is the filtration time for the separation process. The oil removal efficiency, R (%), was calculated according to Eq. (7):

$$R = \left(1 - \frac{C_p}{C_f}\right) \times 100\% \tag{7}$$

In Eq. (7), C_p (ppm) and C_f (ppm) are the oil content of the permeate and feed, respectively.

3. Results and discussion

3.1. Morphology control of ceramic microsheets

Fig. 1 shows the digital photos of the thin ceramic green bodies and ceramic microsheets. The ceramic green bodies, as thin as 0.226 mm, showed relatively uniform surfaces with micrometer-scale surface roughness (Figures S4 and S5, ESI-4) and considerable flexibility due to the existence of PSf (Fig. 1a–c). Ceramic microsheets were achieved with a thickness of 0.192 mm, and also showed a smooth surface but a rigid planar shape after the polymer phase had burned off (Fig. 1d–f).

Fig. 2 shows the cross-sectional evolution of SEM morphologies for the ceramic green bodies during the temperature-programed sintering process. Typical finger-like (Fig. 2a–c) and sponge-like (Fig. 2d–f) cross-sectional morphologies were obtained via typical non-solvent-induced phase separation (NIPS) using a coagulation bath of water and ethanol, respectively, due to the different phase inversion rates. In addition, a relatively denser sponge-like cross-sectional morphology (Fig. 1g–i) was also fabricated using a process that combined solvent evaporation-induced phase separation and the following NIPS method in water. Based on the thermal decomposition properties of PSf and PSf/Al_2O_3 composite films (ceramic green bodies), a calcination temperature of 600 °C was sufficient to burn off the polymer phase that was uniformly distributed around Al_2O_3 particles (Figure S1, ESI-1). After calcination at 600 °C under air, the Al_2O_3 particles generated an intermediate ceramic microsheet (Fig. 1b, e, and h) with almost the same cross-sectional morphology as the ceramic green bodies, which indicates that the final microstructure can be primarily controlled via the phase-inversion process of polymers. Indeed, even after calcination at 1,250 °C for 2 h under air, all the types of intermediate ceramic microsheets retained their cross-sectional morphologies with no structure destruction, regardless of whether the morphology was finger-like or sponge-like. During the sintering process from virgin PSf/Al_2O_3 films to the final ceramic microsheets, we observed a decrease in thickness for these three types of ceramic microsheets due to the shrinking effect of the Al_2O_3 phase. Typically, both the ratio of ceramic/polymer and the sintering temperature play important roles in the shrinking ratio as well as pore size and mechanical strength of ceramic membranes [23–25]. Generally, both a higher ceramic/polymer ratio and a higher sintering temperature ($>$ 1,000 °C) should be considered to guarantee the formation of integrated, porous membranes with sufficient mechanical strength. In addition, the viscosity that can be significantly affected by the ceramic/polymer ratio plays an important role in the formation of either a finger-like or sponge-like structure. A threshold viscosity is then defined as the viscosity where the finger-like structure turns into a sponge-like version in a typical coagulation bath of water [23]. In the present study, a suspension of PSf/Al_2O_3/NMP with a viscosity lower than the threshold value was employed to prepare microsheet membranes with either finger-like or sponge-like structures.

The detailed cross-sectional morphologies and shrinking effect of these achieved ceramic microsheets are shown in Fig. 3. Ceramic microsheets with a finger-like morphology typically show an asymmetric structure with a very thin, dense skin layer that has a considerable amount of finger-like microvoids underneath (Fig. 3a–b). There were also many smaller holes, or pores, on the walls of the finger-like microvoids due to the template effect of the polymer (PSf and F-127) microphase that acted as binding, dispersing, pore-forming, and structure-directing agents. In a similar manner, ceramic microsheets with a sponge-like structure also presented a large number of small holes, or pores, in their cross-sectional surface, but without the presence of larger microvoids (Fig. 3d–e). It is worth noting that the size for the holes or pores from the top to bottom in the cross-sectional surface was gradually increased and formed a slightly asymmetric cross-sectional morphology due to the uneven distribution of the polymer phase during the phase-inversion process. However, in the case of ceramic microsheets with a denser sponge-like structure, no obvious difference in the size of holes or pores from the top to bottom in the cross-sectional surface was observed (Fig. 3g–h). This phenomenon is generally due to the relatively uniform phase inversion rate of the polymer phase induced by

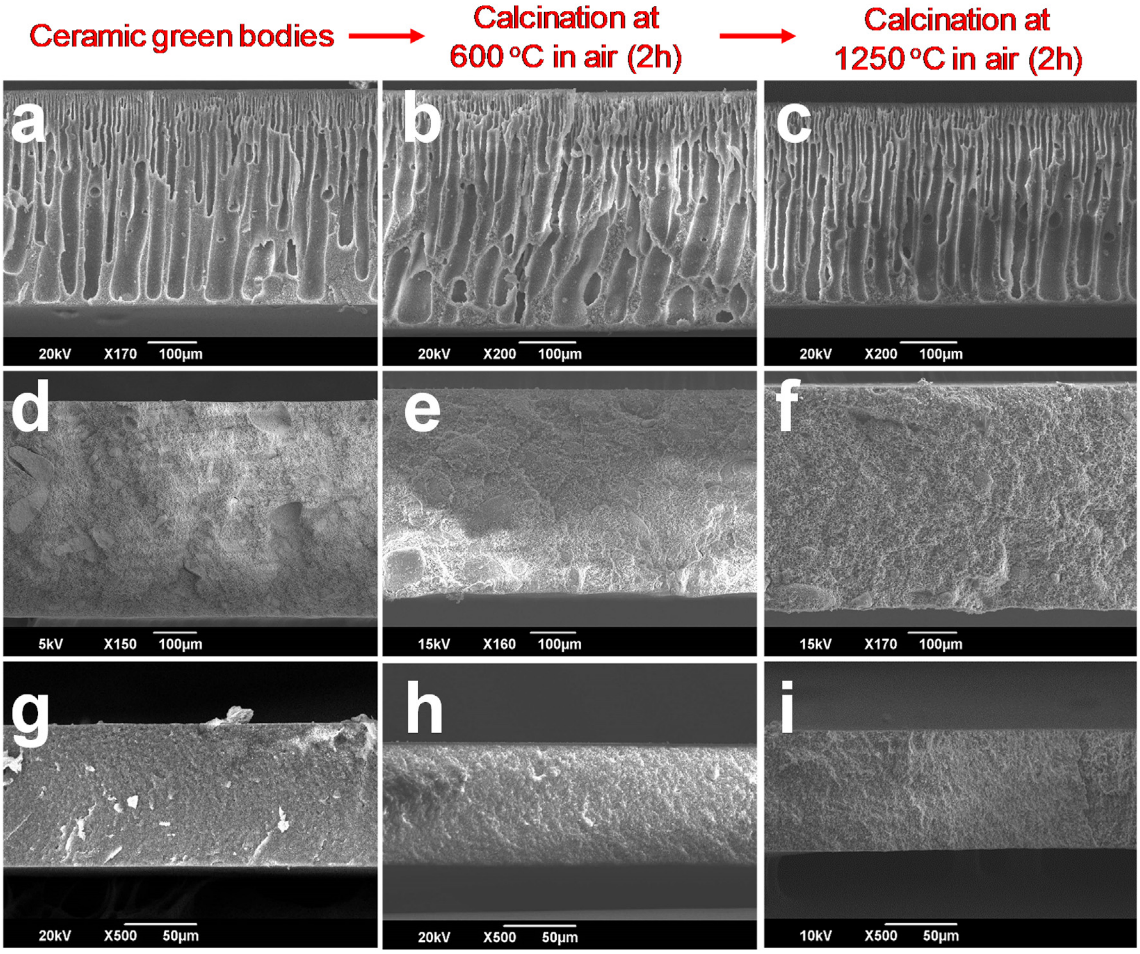

Fig. 2. Morphology involution with calcination temperatures for ceramic green bodies fabricated via phase inversion in a coagulation bath of (a–c) water and (d–f) ethanol at 25 °C, and (g–i) solidification under air at 50 °C for 60 min with further phase inversion in a coagulation bath of water for detachment.

solvent evaporation under air [26–28]. The shrinking effects in the dimensions of both thickness (Fig. 3c, f, and j) and diameter (not shown) for these three types of ceramic microsheets were studied. No differences were observed in the shrinking ratios (~11%) of the circular diameters of these ceramic microsheets due to the formation of a closely packed skin layer in all types of ceramic microsheets. By comparing the thicknesses of the ceramic green bodies and the final ceramic microsheets, however, clear differences were detected in the shrinking ratios of thickness among the ceramic microsheets. All three types of ceramic microsheets demonstrated almost linear relationships in thickness between ceramic green bodies and the final ceramic microsheets (Fig. 3c, f, and i). Calculation of the shrinking ratios showed a descending order: finger-like (26%) > sponge-like (12%) > dense sponge-like (10%). This order was the opposite of that for mechanical strength based on the calculation of critical stresses at rupture: finger-like (5–25 MPa) < sponge-like (40–80 MPa) < dense sponge-like (80–120 MPa) (Table S1, ESI-5). In addition, the cross-sectional morphologies of the sponge-like structure can be further tuned by controlling the hold-up duration of the cast semi-solid film before immersion in a coagulation bath. By extending the hold-up duration, the thickness of the dense-packing region was increased from 2 µm for 0 min to an entire range (200–400 µm) for 60 min (Figure S3, ESI-3).

In addition to the cross-sectional morphologies, the surface morphologies of these ceramic microsheets were also observed using SEM images, as shown in Fig. 4. These ceramic microsheets presented uniform, relatively smooth surfaces without cracks. Compared with the bottom surfaces (Fig. 4d–f), the top surface of each ceramic microsheet (Fig. 4a–c) was relatively denser without the larger pores observed on its bottom surface. The morphologies of the bottom surfaces were relative to the cross-sectional morphologies induced by the phase inversion process of the ceramic green bodies. The ceramic microsheets with either finger-like or sponge-like structures and a relatively loose Al_2O_3 packing density showed larger pores in their bottom surfaces (Fig. 4d–e). However, ceramic microsheets with a dense sponge-like structure showed no clear differences between the top and bottom surfaces due to similar Al_2O_3 packing densities from top to bottom in the cross-sectional structure, as mentioned above.

3.2. Gas permeation properties and structural analysis

Based on the SEM images of these ceramic microsheets, no meso-to-macro pores could be clearly observed on the top surface that would be a selective layer for the separation of liquid mixtures. Therefore, the membrane performance in terms of the permeation flux and the presence of micropores in the ceramic microsheets was further analyzed based on gas permeation tests at different transmembrane pressures. Based on the gas permeation behaviors, Eq. (8) can be used to estimate the average pore radius (r_g) of the ceramic microsheets by considering the contributions that Knudsen and viscous flows make to the overall membrane flux [29–31].

$$K = \frac{Q}{A\Delta p} = 2.133\frac{\nu r_g}{l p_2}\frac{\varepsilon}{q^2} + 1.6\frac{r_g^2}{l\eta p_2}\frac{\varepsilon}{q^2}p_{ave} \tag{8}$$

In Eq. (8), K (m/s) is the effective permeation factor, Q (mol/s) is the molar flow rate, p_2 (Pa) is the pressure in the permeate, while p_{ave} (Pa) is the average pressure across the membrane, ν (m/s) is the

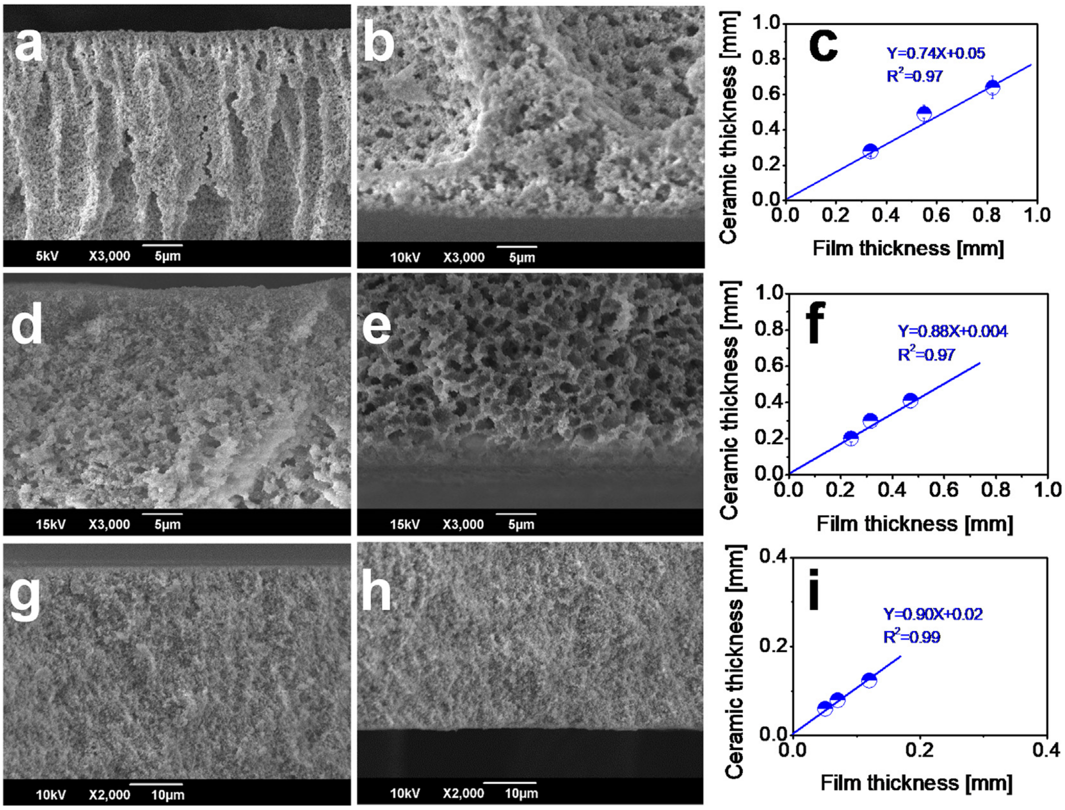

Fig. 3. Cross-sectional morphologies of ceramic microsheets derived from different green bodies and the correlations of the thickness between green bodies and ceramic microsheets: phase inversion in a coagulation bath of (a–c) water and (d–f) ethanol at 25 °C, and (g–i) solidification under air at 50 °C for 60 min and further phase inversion in a coagulation bath of water for detachment.

molecular mean velocity of the gas, η (Pa s) is the viscosity of the gas, q is the tortuosity of the pore channels, and ε/q^2 can be regarded as the effective porosity of the membranes. The first term in eq. (8) is relative to the contribution by *Knudsen* permeance while the second term corresponds to the contribution from viscous permeance. The average pore radius can be obtained from the slope $(1.6\frac{r_g^2}{l\eta p_2}\frac{\varepsilon}{q^2})$ and the intercept $(2.133\frac{\nu r_g}{l p_2}\frac{\varepsilon}{q^2})$ of the linear relationship between K and p_{ave}.

Fig. 5 shows the N_2 permeation properties and the relative structural analysis for these ceramic microsheets with good quality and mechanical strength. The N_2 flux of the selected ceramic microsheets was directly proportional to the transmembrane pressure, indicating the good qualities of these ceramic microsheets (Fig. 5a). Due to increases in the average packing density of Al_2O_3 particles, as observed in the cross-sectional morphologies (Fig. 3), the N_2 flux had the following order: AO-W (finger-like) > AO-E (sponge-like) > AO-A (dense sponge-like). In addition, good linear relationships existed between the effective permeation factor and average pressure for these ceramic microsheets (Fig. 5b). The average pore radii (r_g) calculated based on these plots together with the average N_2 permeance under tested pressures are summarized in Fig. 5c. As expected, the levels of N_2 permeance for these ceramic microsheets were not only relative to the

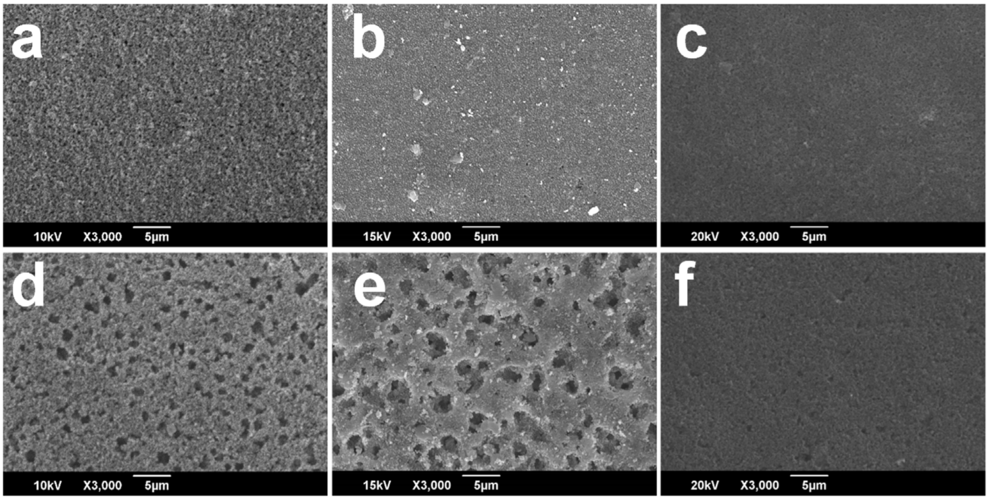

Fig. 4. (a–c) Top and (d–f) bottom surface morphologies for ceramic microsheets derived from different ceramic green bodies: phase inversion in a coagulation bath of (a, d) water and (b, e) ethanol, and (c, f) solidification under air at 50 °C for 60 min and further phase inversion in a coagulation bath of water for detachment.

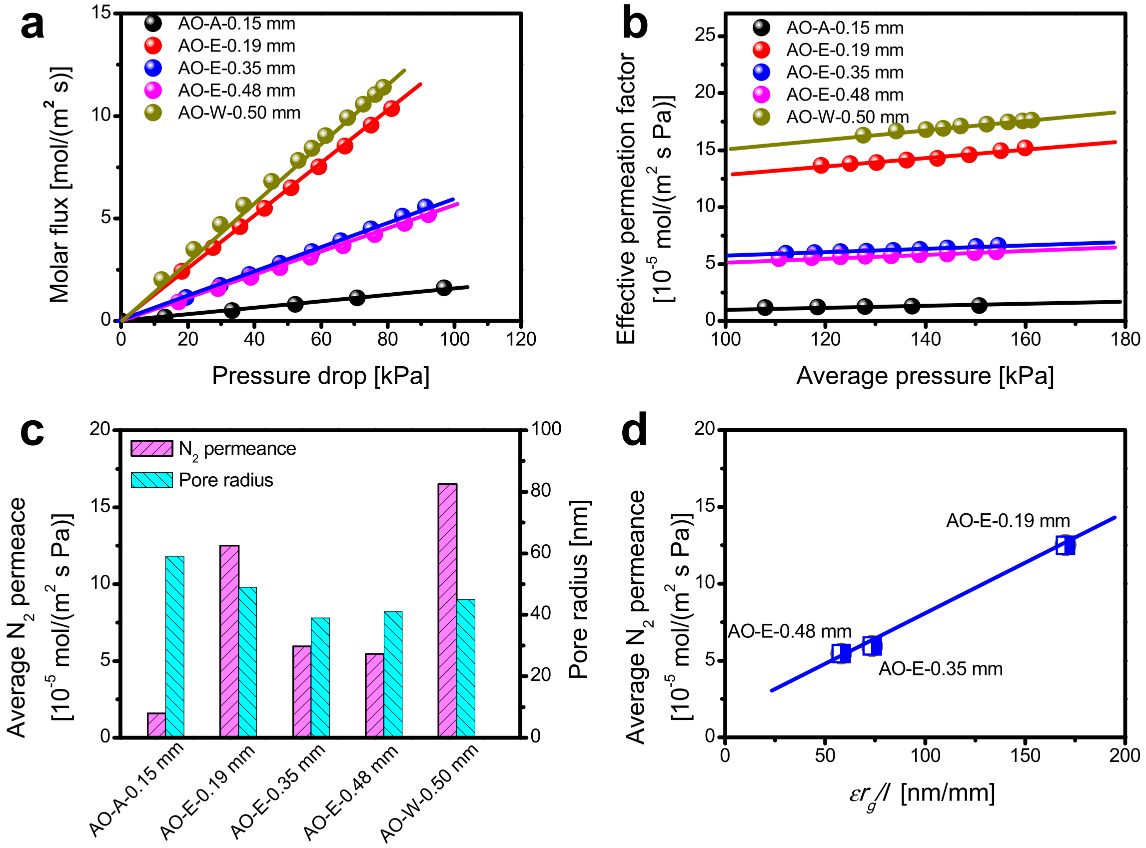

Fig. 5. Gas permeation properties and structural analysis of ceramic microsheets derived from various types of green bodies: (a) N_2 flux at different *trans*-membrane pressure drops, (b) effective permeation factor (*K*) of N_2 at different average pressure drops, (c) N_2 permeance and pore radius calculated based on gas permeation, and (d) correlations between membrane structural parameters ($\varepsilon r_g/l$) and N_2 permeance.

packing densities of Al_2O_3 particles (cross-sectional morphologies) but also were correlated with the thicknesses of the ceramic microsheets. The thinner the ceramic microsheets, the higher the N_2 permeance. There was no obvious correlation between the pore radius and the thickness of the ceramic microsheets. This was probably because the pore radius of the ceramic microsheets is primarily controlled by the size of Al_2O_3 particles in the topmost dense packing layer and by the final sintering temperature. All the ceramic microsheets demonstrated comparable values in pore radii (ca. 39–59 nm) and a high-level porosity of ca. 55–78% (Table S1, ESI-5), which is almost 2-fold higher than most reported ceramic MF membranes. Based on the *Hagen-Poiseuille* equation, such high-level porosity together with a thickness of sub-0.5 mm would reasonably contribute to a much higher permeation flux of liquids by comparison with ceramic membranes of similar pore sizes. Interestingly, the observed porosity tended to follow the order of the packing density of Al_2O_3 particles regardless of the thickness of the ceramic microsheets. It should be mentioned that these ceramic microsheets presented a *Knudsen*-dominant (50–80%) permeation flux of N_2 (Table S1, ESI-5), which could have been due to the relatively smaller pore radius as well as to the good quality of the ceramic microsheets. In addition, the permeability of a certain penetrating species can be generally expressed and predicted by the membrane structural parameters such as surface porosity (ε), pore radius (r_p), and pore/membrane thickness (l). Typically, the permeance is positively proportional to the surface porosity and pore radius while negatively proportional to the membrane thickness, $P \propto \varepsilon r/l$. Fig. 5d depicts the correlation between N_2 permeance and membrane structural parameters ($\varepsilon r_g/l$) for these ceramic microsheets with sponge-like structures (AO-E). A good proportional relationship was observed, which indicated the good qualities of the ceramic microsheets. Given that the AO-E type ceramic microsheets tended to exhibit a complex combination of high mechanical strength, high gas flux, and good quality, these ceramic microsheets were further studied for the separation of oil-in-water emulsions.

3.3. Surface wettability and emulsified oil/water separation properties

To probe the surface wettability of the ceramic microsheets, we conducted the measurements of static water and oil contact angles under air and underwater dynamic oil adhesion testing, and observed the underwater sliding behaviors of oil droplets. Water droplets spread quickly on the ceramic microsheets, perhaps due to the hydrophilicity and high-porosity surface of the packed Al_2O_3 particles (Fig. 6a). In a similar development, the mineral oil contact angle on the surface of the ceramic microsheets under air was as low as 17.3° (Fig. 6b), which indicated an apparent amphiphilic-like surface structure. Once the ceramic microsheets were placed under water, however, superoleophobic properties were observed based on the dynamic oil adhesion and sliding tests using CCl_4 droplets (Fig. 6c and d). A dynamic “pre-load-compress-lift up” test showed that the oil droplets, with a static contact angle of ∼150 °C under water, could be easily and gently withdrawn from the surface of the ceramic microsheets via a dispensing metal needle with a very weak drag force. In addition, a very small roll-off angle of 2.8° was also observed during the underwater sliding test (Fig. 6d), which indicated a relatively higher quality of the superoleophobic surface. Generally, water molecules are trapped in the rough micro/nanostructures on a hydrophilic surface with high surface energy under water, and the increased hydrophilicity of the interface increases the underwater oleophobicity. Indeed, in most cases, the superhydrophilic surface also possesses underwater superoleophobic properties [32]. Generally, a superhydrophobic surface exhibits a roll-off angle of < 5°, and very high-quality superhydrophobic surfaces

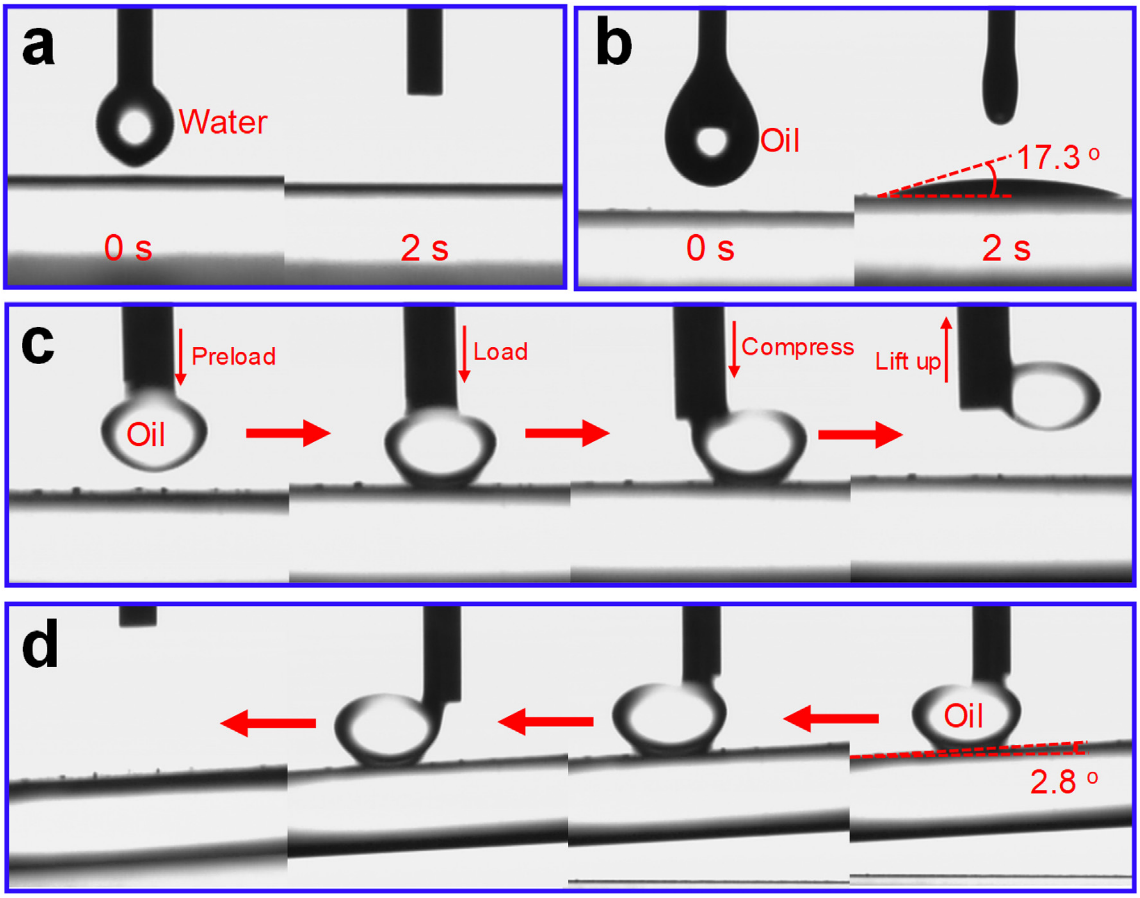

Fig. 6. Surface wettability of ceramic microsheets derived from phase inversion in a coagulation bath of ethanol at 25 °C: (a) fast spreading of water droplets and (b) a lower oil contact angle under air; (c) underwater dynamic oil adhesion process; (d) underwater sliding behavior of oil droplets with a roll-off angle of 2.8°.

have roll-off angles as low as 1° [33,34]. It should be noted that such superoleophobic surface properties would play an important role in the high-quality separation of oil-in-water emulsions as well as in the anti-fouling properties of oil droplets.

Pure water flux was conducted at various transmembrane pressures using selected ceramic microsheets (AO-E – 0.19 mm and AO-E – 0.48 mm). Good linear relationships between pure water flux and the transmembrane pressure drop were observed for ceramic microsheets AO-E – 0.19 mm and AO-E – 0.48 mm, and very attractive pure water permeability values of 40,956 L/(m^2 h bar) and 13,562 L/(m^2 h bar), respectively, were obtained from the slopes (Fig. 7a). Such high-water permeability for these ceramic microsheets was expected and shows great promise for the treatment of large amounts of industrial oily wastewater in a continuous cross-flow membrane unit. To evaluate the separation capabilities of oily wastewater for these ceramic microsheets, a surfactant-stabilized oil-in-water emulsion with an oil concentration of 1,000 ppm and a uniform oil droplet size of 1,000 nm was prepared as a simulated separation mixture (Fig. 7b and e). The steady-state separation properties in terms of emulsion permeabilities and separation efficiency at a transmembrane pressure of 0.1 MPa are summarized in Fig. 7c. Generally, an initially fast decline in emulsion permeability can be observed for the first 10–30 min before reaching a relatively stable level of permeability (Figure S10, ESI-7). The ceramic microsheets simultaneously exhibited a highly impressive steady-state permeability that ranged from 2,300–3,000 L/(m^2 h bar) and a high separation efficiency of > 99%. The thinner ceramic microsheets (AO-E – 0.19 mm, 2,958 L/(m^2 h bar)) demonstrated a slightly higher level of stable permeability compared with the thicker ones (AO-E – 0.48 mm, 2,318 L/(m^2 h bar)), probably due to the reduced pore blocking effect that was the result of either the reduced thickness or the length of the pores. Indeed, membrane fouling by the pore blocking effect and cake layer formation is a very serious and almost inevitable phenomenon for oil/water separation applications [35–37]. Dynamic membrane fouling behaviors were achieved with the ceramic microsheets (AO-E – 0.19 mm), as illustrated in Fig. 7d. The permeation flux of the emulsion declined steeply once the oil-in-water emulsion was fed into the membrane unit from an initial value of ~40,000 L/(m^2 h bar) to a stable value of ~2,900 L/(m^2 h bar) within 60 min of the first filtration circle. However, after an in-situ regeneration process via the filtration of 500 mL of an SDS solution (1,000 ppm) and a subsequent 500 mL of hot ethanol (50 °C) at 0.02 MPa, the permeation flux for a second circle had almost recovered with a stable value that was comparable to the first filtration circle. In addition, high-quality separation of oil-in-water emulsions was directly observed based on the transparency of the emulsions before and after filtration (Fig. 7e) and on the corresponding distribution of oil droplets on the silicon wafer (Fig. 7f and g). After filtration, the emulsion solution was very clear and transparent (Fig. 7e) and almost no oil droplets were observed (Fig. 7g). The much smaller particle size of ~4 nm in the permeate solution, as measured by DLS, can be ascribed to the free SDS molecules and/or to a very few oil molecules.

The pure water permeability and the separation capabilities for emulsified oil/water mixtures of these ceramic microsheets in the present study were compared with those in the literature, as illustrated in Fig. 8 (see details in Tables S2 and S3, ESI-8) [38–46]. The reported conventional ceramic MF membranes were generally prepared via a multi-step sintering process, which included the sintering of a macroporous ceramic support at high temperature and the subsequent development of an active MF layer on the support. Such processes always increase the levels of energy consumption and the need for raw

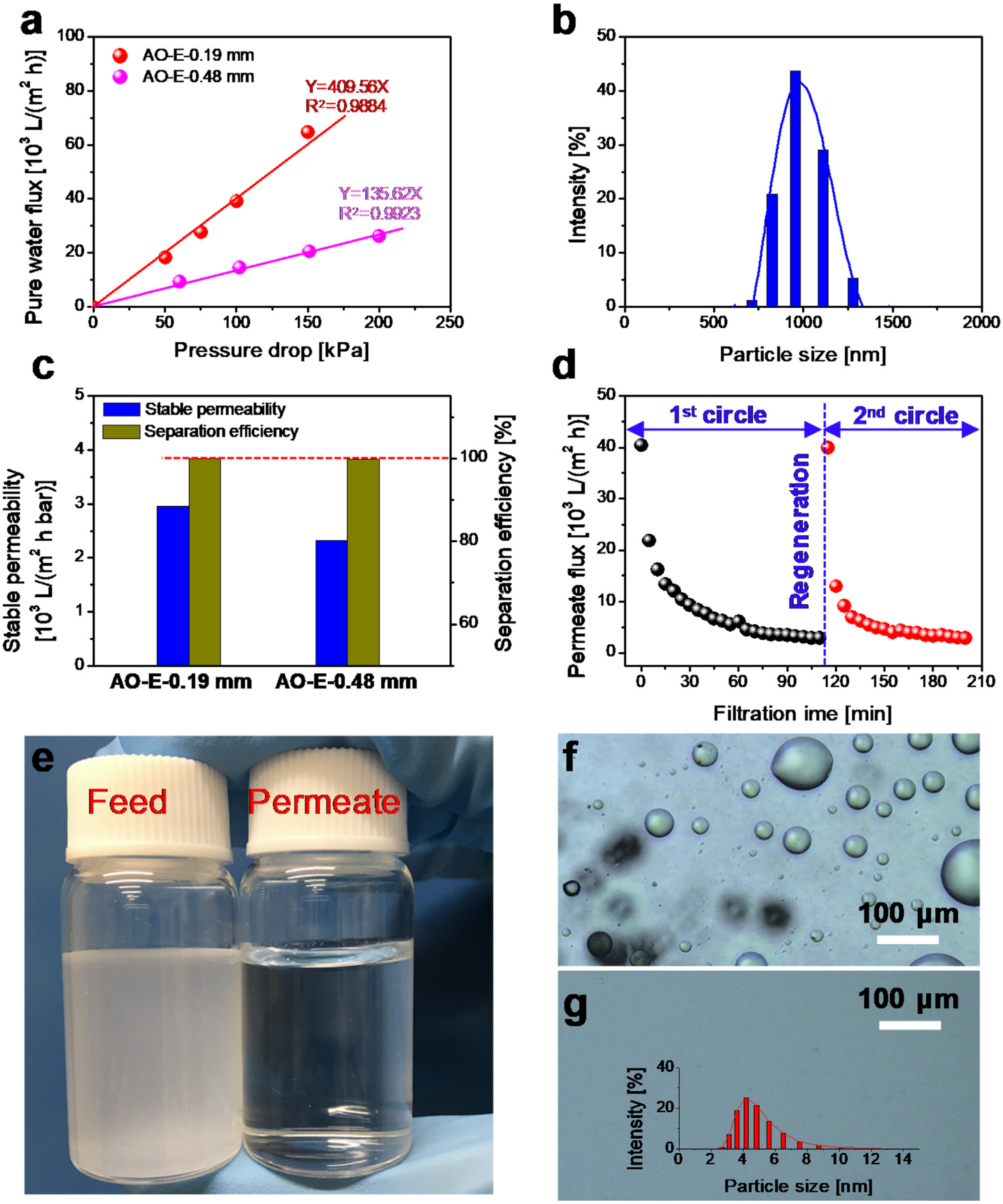

Fig. 7. Pure water permeation and emulsified oil/water separation performance of the ceramic microsheets derived from phase inversion in a coagulation bath of ethanol at 25 °C: (a) pure water permeation flux at various transmembrane pressures; (b) particle size distribution of emulsified oil droplets in water; (c) separation properties in terms of stable permeability and separation efficiency for oil-in-water emulsions at 0.1 MPa; (d) permeation flux *vs.* filtration time during the separation of oil-in-water emulsions for AO-E – 0.19 mm (the ceramic microsheets were in-situ regenerated by the filtration of 500 mL SDS aqueous solutions and 500 mL hot ethanol at 0.02 MPa); (e) the appearance of the feed and permeate solution; (f) the optical images of the oil-in-water emulsions in the feed on a silicon wafer; and, (g) the optical images of the oil-in-water emulsions in the permeate on a silicon wafer with the droplet size distribution based on DLS shown in the inset.

materials that are much more expensive than the ceramic microsheets. In addition to this, by comparing with conventional MF membranes regardless of the variations in the pore sizes that ranged from 50 to 500 nm, these low-cost microsheet membranes demonstrated outstanding water permeation performance (Fig. 8a and Table S2), which can be explained by the diminished thickness of the entire microsheet and the active separation layer, as well as by the high level of porosity. Moreover, even compared with most reported alumina hollow fiber membranes with a similar level of pore size prepared via a similar phase inversion/sintering method, the ceramic microsheet membranes still showed higher pure water permeability (Table S2, ESI-8). The pure water permeability of these reported ceramic MF membranes can be

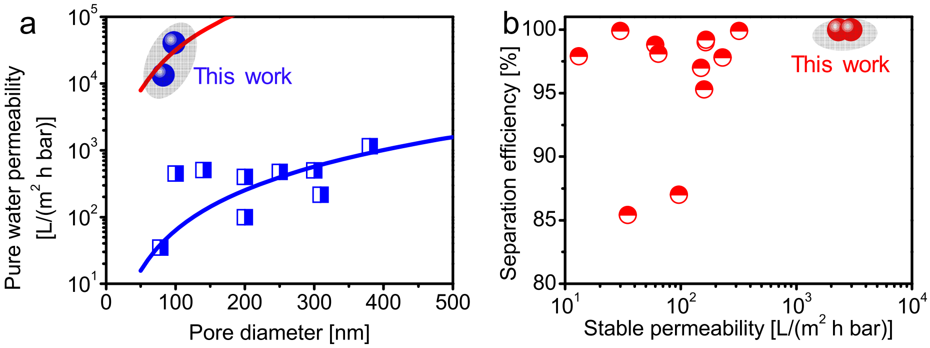

Fig. 8. Performance of ceramic microsheets compared with that reported for ceramic MF membranes: (a) relationships of pure water permeability *vs.* pore diameter with estimated water permeability based on the Hagen-Poiseuille equation shown by the solid lines, which assumes a porosity of 50% with a thickness of 1 mm (blue line) and 0.005 mm (red line); and, (b) relationships of separation efficiency *vs.* stable permeability for the separation of oil-in-water emulsions.

roughly estimated using the Hagen-Poiseuille equation by assuming an active thickness of 1 mm with a porosity of 50%. An active thickness for the ceramic microsheets was estimated to approximate 0.005 mm with the same level of porosity. Furthermore, compared with most ceramic MF membranes (and polymeric MF membranes shown in Table S3, ESI-8) when used for emulsified oil-in-water separation [38,47–58], the ceramic microsheets also exhibited a much higher stable emulsion flux with an extremely high separation efficiency of > 99% (Fig. 8b). These microsheet membranes also demonstrated superior cycling performance after several cycles without an obvious decline in performance (Figure S11, ESI-7). In addition, it is important to note that compared with commercially available Anodic Aluminum Oxide (AAO) membranes (pore size, ~200 nm) that have an ultrathin thickness, and a honeycomb-like microstructure with very uniform pore size, the low-cost, ceramic microsheet membranes could still perform better in terms of the stable permeation flux of oil/water emulsions (Table S3 and Figure S12, ESI-8). AAO membranes although with a very high initial pure water flux demonstrated a serious decline in permeation flux for the first 1 h and then maintained a lower stable value. This indicates that the ceramic microsheet membranes demonstrated a better antifouling properties for the emulsified oil/water mixture probably due to the asymmetric sponge-like microstructure and underwater superoleophobic properties that significantly reduced the cake layer formation on the membrane surface and the pore blocking effect. Consequently, the ceramic microsheet membranes could maintain a high-level emulsion flux for a longer period of time without a serious decline in flux as seen in AAO or most reported membranes, which thus reduces the time and cost for washing/regeneration. Furthermore, the ceramic microsheet membranes made of α-Al_2O_3 were more hydrothermally stable than the AAO membranes that have an amorphous microstructure. Therefore, such flat-sheet membranes with sufficient mechanical strength, low cost, superior separation and antifouling properties are expected to have valuable applications in aqueous- and nonaqueous-based separations in addition to oil/water separations, such as protein-based separations in food and medical fields, and as lab-scale inorganic filters. In addition, if appropriately supported, these microsheet membranes could also be installed to plate and frame modules to further reduce membrane fouling, blocking, and permeation resistance compared with hollow fiber ceramic membranes.

4. Conclusions

Low-cost ceramic microsheets with a thickness of sub-0.5 mm were developed using a slurry consisting of PSf and Al_2O_3 particles via phase inversion/sintering. The obtained microsheets can be as thin as 0.19 mm with good integrity and mechanical strength for use in MF membrane separation. Different phase inversion media (water, ethanol, and air) were employed to tailor the cross-sectional morphologies (finger-like or sponge-like) of the ceramic green bodies, which retained their microstructures in the resultant ceramic microsheets following a high-temperature (1,250 °C) sintering process. These microsheet membranes presented a pore size ranging from 80 to 120 nm that can be primarily decided by both Al_2O_3 particle size (~200 nm) and the sintering temperature, irrespective of the cross-sectional morphologies, due to the formation of a dense skin layer on the topmost surface. In addition, these microsheet membranes exhibited superhydrophilic and underwater superoleophobic properties and therefore demonstrated great potential for oil/water mixtures or emulsions. This super-wetting ability combined with a thin nature (sub-0.5 mm), a desireable level of surface porosity (50–80%), and a suitable pore size (80–120 nm) simultaneously endowed the microsheet membranes with attractive pure water (13,000–41,000 L/(m^2 h bar)) and oil/water emulsion (2,300–3,000 L/(m^2 h bar)) fluxes and outstanding oil-removal efficiency (> 99%). Low cost and a level of emulsion flux that is 2 orders of magnitude higher than most commercially available microfiltration membranes with similar oil-removal efficiency, makes these ceramic microsheet membranes very promising for the high-quality separation of industrial oily wastewater under complex chemical conditions.

Notes

The authors declare no competing financial interests.

Appendix A. Supplementary data

Supplementary data to this article can be found online at https://doi.org/10.1016/j.memsci.2019.117477.

References

[1] M. Padaki, R.S. Murali, M.S. Abdullah, N. Misdan, A. Moslehyani, M. Kassim, N. Hilal, A. Ismail, Membrane technology enhancement in oil–water separation. A review, Desalination 357 (2015) 197–207.
[2] J.A. Veil, M.G. Puder, D. Elcock, R.J. Redweik Jr., A white paper describing produced water from production of crude oil, natural gas, and coal bed methane, Argonne National Lab., IL (US), 2004.
[3] M. Cheryan, N. Rajagopalan, Membrane processing of oily streams. Wastewater treatment and waste reduction, J. Membr. Sci. 151 (1998) 13–28.
[4] P. Janknecht, A.D. Lopes, A.M. Mendes, Removal of industrial cutting oil from oil emulsions by polymeric ultra-and microfiltration membranes, Environ. Sci. Technol. 38 (2004) 4878–4883.
[5] R.K. Gupta, G.J. Dunderdale, M.W. England, A. Hozumi, Oil/water separation techniques: a review of recent progresses and future directions, J. Mater. Chem. A 5 (2017) 16025–16058.
[6] H.J. Tanudjaja, C.A. Hejase, V.V. Tarabara, A.G. Fane, J.W. Chew, Membrane-Based Separation for Oily Wastewater: A Practical Perspective, Water Res., 2019.
[7] Z. Xue, Y. Cao, N. Liu, L. Feng, L. Jiang, Special wettable materials for oil/water separation, J. Mater. Chem. A 2 (2014) 2445–2460.
[8] D. Tian, X. Zhang, Y. Tian, Y. Wu, X. Wang, J. Zhai, L. Jiang, Photo-induced water–oil separation based on switchable superhydrophobicity–superhydrophilicity and underwater superoleophobicity of the aligned ZnO nanorod array-coated mesh films, J. Mater. Chem. 22 (2012) 19652–19657.
[9] Q. Wen, J. Di, L. Jiang, J. Yu, R. Xu, Zeolite-coated mesh film for efficient oil–water separation, Chem. Sci. 4 (2013) 591–595.
[10] C. Lee, S. Baik, Vertically-aligned carbon nano-tube membrane filters with superhydrophobicity and superoleophilicity, Carbon 48 (2010) 2192–2197.
[11] J. Song, S. Huang, Y. Lu, X. Bu, J.E. Mates, A. Ghosh, R. Ganguly, C.J. Carmalt, I.P. Parkin, W. Xu, Self-driven one-step oil removal from oil spill on water via selective-wettability steel mesh, ACS Appl. Mater. Interfaces 6 (2014) 19858–19865.

[12] A. Huang, L.-H. Chen, C.-C. Kan, T.-Y. Hsu, S.-E. Wu, K.K. Jana, K.-L. Tung, Fabrication of zinc oxide nanostructure coated membranes for efficient oil/water separation, J. Membr. Sci. 566 (2018) 249–257.

[13] A. Huang, C.-C. Kan, S.-C. Lo, L.-H. Chen, D.-Y. Su, J.F. Soesanto, C.-C. Hsu, F.-Y. Tsai, K.-L. Tung, Nanoarchitectured design of porous ZnO@ copper membranes enabled by atomic-layer-deposition for oil/water separation, J. Membr. Sci. 582 (2019) 120–131.

[14] Y. Si, Q. Fu, X. Wang, J. Zhu, J. Yu, G. Sun, B. Ding, Superelastic and superhydrophobic nanofiber-assembled cellular aerogels for effective separation of oil/water emulsions, ACS Nano 9 (2015) 3791–3799.

[15] G.J. Dunderdale, C. Urata, T. Sato, M.W. England, A. Hozumi, Continuous, high-speed, and efficient oil/water separation using meshes with antagonistic wetting properties, ACS Appl. Mater. Interfaces 7 (2015) 18915–18919.

[16] M. Çakmakce, N. Kayaalp, I. Koyuncu, Desalination of produced water from oil production fields by membrane processes, Desalination 222 (2008) 176–186.

[17] K.A. DeFriend, M.R. Wiesner, A.R. Barron, Alumina and aluminate ultrafiltration membranes derived from alumina nanoparticles, J. Membr. Sci. 224 (2003) 11–28.

[18] J. Luyten, A. Buekenhoudt, W. Adriansens, J. Cooymans, H. Weyten, F. Servaes, R. Leysen, Preparation of LaSrCoFeO3− x membranes, Solid State Ion. 135 (2000) 637–642.

[19] B.F. Kingsbury, K. Li, A morphological study of ceramic hollow fibre membranes, J. Membr. Sci. 328 (2009) 134–140.

[20] M. Lee, B. Wang, K. Li, New designs of ceramic hollow fibres toward broadened applications, J. Membr. Sci. 503 (2016) 48–58.

[21] B. Wang, Z. Lai, Finger-like voids induced by viscous fingering during phase inversion of alumina/PES/NMP suspensions, J. Membr. Sci. 405 (2012) 275–283.

[22] N. Abdullah, M.A. Rahman, M.H.D. Othman, A. Ismail, J. Jaafar, A.A. Aziz, Preparation and characterization of self-cleaning alumina hollow fiber membrane using the phase inversion and sintering technique, Ceram. Int. 42 (2016) 12312–12322.

[23] S.K. Hubadillah, M.H.D. Othman, T. Matsuura, A. Ismail, M.A. Rahman, Z. Harun, J. Jaafar, M. Nomura, Fabrications and applications of low cost ceramic membrane from kaolin: a comprehensive review, Ceram. Int. 44 (2018) 4538–4560.

[24] S.K. Hubadillah, Z. Harun, M.H.D. Othman, A. Ismail, W.N.W. Salleh, H. Basri, M.Z. Yunos, P. Gani, Preparation and characterization of low cost porous ceramic membrane support from kaolin using phase inversion/sintering technique for gas separation: effect of kaolin content and non-solvent coagulant bath, Chem. Eng. Res. Des. 112 (2016) 24–35.

[25] R. Sarbatly, Z. Kamin, The effects of Kaolin/PESF Ratios on the microstructures of kaolin hollow tubes, Developments in Sustainable Chemical and Bioprocess Technology, Springer, 2013, pp. 381–387.

[26] P. Van de Witte, P. Dijkstra, J. Van den Berg, J. Feijen, Phase separation processes in polymer solutions in relation to membrane formation, J. Membr. Sci. 117 (1996) 1–31.

[27] I. Wienk, R. Boom, M. Beerlage, A. Bulte, C. Smolders, H. Strathmann, Recent advances in the formation of phase inversion membranes made from amorphous or semi-crystalline polymers, J. Membr. Sci. 113 (1996) 361–371.

[28] J.T. Jung, J.F. Kim, H.H. Wang, E. Di Nicolo, E. Drioli, Y.M. Lee, Understanding the non-solvent induced phase separation (NIPS) effect during the fabrication of microporous PVDF membranes via thermally induced phase separation (TIPS), J. Membr. Sci. 514 (2016) 250–263.

[29] J. Marchese, C. Pagliero, Characterization of asymmetric polysulphone membranes for gas separation, Gas Sep. Purif. 5 (1991) 215–221.

[30] M. Almandoz, J. Marchese, P. Prádanos, L. Palacio, A. Hernández, Preparation and characterization of non-supported microfiltration membranes from aluminosilicates, J. Membr. Sci. 241 (2004) 95–103.

[31] B. Nandi, R. Uppaluri, M. Purkait, Preparation and characterization of low cost ceramic membranes for micro-filtration applications, Appl. Clay Sci. 42 (2008) 102–110.

[32] J. Ge, J. Zhang, F. Wang, Z. Li, J. Yu, B. Ding, Superhydrophilic and underwater superoleophobic nanofibrous membrane with hierarchical structured skin for effective oil-in-water emulsion separation, J. Mater. Chem. A 5 (2017) 497–502.

[33] A. Marmur, The lotus effect: superhydrophobicity and metastability, Langmuir 20 (2004) 3517–3519.

[34] W. Choi, A. Tuteja, J.M. Mabry, R.E. Cohen, G.H. McKinley, A modified Cassie–Baxter relationship to explain contact angle hysteresis and anisotropy on non-wetting textured surfaces, J. Colloid Interface Sci. 339 (2009) 208–216.

[35] K. He, H. Duan, G.Y. Chen, X. Liu, W. Yang, D. Wang, Cleaning of oil fouling with water enabled by zwitterionic polyelectrolyte coatings: overcoming the imperative challenge of oil–water separation membranes, ACS Nano 9 (2015) 9188–9198.

[36] Y. Zhu, D. Wang, L. Jiang, J. Jin, Recent progress in developing advanced membranes for emulsified oil/water separation, NPG Asia Mater. 6 (2014) e101.

[37] A.K. Kota, G. Kwon, W. Choi, J.M. Mabry, A. Tuteja, Hygro-responsive membranes for effective oil–water separation, Nat. Commun. 3 (2012) 1025.

[38] D. Zou, M. Qiu, X. Chen, E. Drioli, Y. Fan, One step co-sintering process for low-cost fly ash based ceramic microfiltration membrane in oil-in-water emulsion treatment, Separ. Purif. Technol. 210 (2019) 511–520.

[39] B. Achiou, H. Elomari, A. Bouazizi, A. Karim, M. Ouammou, A. Albizane, J. Bennazha, S.A. Younssi, I. El Amrani, Manufacturing of tubular ceramic microfiltration membrane based on natural pozzolan for pretreatment of seawater desalination, Desalination 419 (2017) 181–187.

[40] Q. Chang, J.-e. Zhou, Y. Wang, J. Wang, G. Meng, Hydrophilic modification of Al2O3 microfiltration membrane with nano-sized γ-Al2O3 coating, Desalination 262 (2010) 110–114.

[41] Y. Yu, W. Hou, X. Hu, Y. Yu, L. Mi, L. Song, Superhydrophobic modification of an Al 2 O 3 microfiltration membrane with TiO 2 coating and PFDS grafting, RSC Adv. 4 (2014) 48317–48321.

[42] I. Jedidi, S. Saïdi, S. Khemakhem, A. Larbot, N. Elloumi-Ammar, A. Fourati, A. Charfi, A.B. Salah, R.B. Amar, Elaboration of new ceramic microfiltration membranes from mineral coal fly ash applied to waste water treatment, J. Hazard Mater. 172 (2009) 152–158.

[43] P. Wang, P. Huang, N. Xu, J. Shi, Y. Lin, Effects of sintering on properties of alumina microfiltration membranes, J. Membr. Sci. 155 (1999) 309–314.

[44] R.V. Kumar, A.K. Ghoshal, G. Pugazhenthi, Elaboration of novel tubular ceramic membrane from inexpensive raw materials by extrusion method and its performance in microfiltration of synthetic oily wastewater treatment, J. Membr. Sci. 490 (2015) 92–102.

[45] Y. Lin, D. Zou, X. Chen, M. Qiu, H. Kameyama, Y. Fan, Low temperature sintering preparation of high-permeability TiO2/Ti composite membrane via facile coating method, Appl. Surf. Sci. 349 (2015) 8–16.

[46] C. Yang, G. Zhang, N. Xu, J. Shi, Preparation and application in oil–water separation of ZrO2/α-Al2O3 MF membrane, J. Membr. Sci. 142 (1998) 235–243.

[47] M. Abbasi, M. Mirfendereski, M. Nikbakht, M. Golshenas, T. Mohammadi, Performance study of mullite and mullite–alumina ceramic MF membranes for oily wastewaters treatment, Desalination 259 (2010) 169–178.

[48] S. Emani, R. Uppaluri, M.K. Purkait, Microfiltration of oil–water emulsions using low cost ceramic membranes prepared with the uniaxial dry compaction method, Ceram. Int. 40 (2014) 1155–1164.

[49] J. Cui, X. Zhang, H. Liu, S. Liu, K.L. Yeung, Preparation and application of zeolite/ceramic microfiltration membranes for treatment of oil contaminated water, J. Membr. Sci. 325 (2008) 420–426.

[50] D. Vasanth, G. Pugazhenthi, R. Uppaluri, Cross-flow microfiltration of oil-in-water emulsions using low cost ceramic membranes, Desalination 320 (2013) 86–95.

[51] D. Zou, J. Xu, X. Chen, E. Drioli, M. Qiu, Y. Fan, A novel thermal spraying technique to fabricate fly ash/alumina composite membranes for oily emulsion and spent tin wastewater treatment, Separ. Purif. Technol. 219 (2019) 127–136.

[52] J. Fang, G. Qin, W. Wei, X. Zhao, L. Jiang, Elaboration of new ceramic membrane from spherical fly ash for microfiltration of rigid particle suspension and oil-in-water emulsion, Desalination 311 (2013) 113–126.

[53] J. Mueller, Y. Cen, R.H. Davis, Crossflow microfiltration of oily water, J. Membr. Sci. 129 (1997) 221–235.

[54] S.R.H. Abadi, M.R. Sebzari, M. Hemati, F. Rekabdar, T. Mohammadi, Ceramic membrane performance in microfiltration of oily wastewater, Desalination 265 (2011) 222–228.

[55] F. Hua, Y. Tsang, Y. Wang, S. Chan, H. Chua, S. Sin, Performance study of ceramic microfiltration membrane for oily wastewater treatment, Chem. Eng. J. 128 (2007) 169–175.

[56] L. Zhu, M. Chen, Y. Dong, C.Y. Tang, A. Huang, L. Li, A low-cost mullite-titania composite ceramic hollow fiber microfiltration membrane for highly efficient separation of oil-in-water emulsion, Water Res. 90 (2016) 277–285.

[57] Q. Chang, J.-e. Zhou, Y. Wang, J. Liang, X. Zhang, S. Cerneaux, X. Wang, Z. Zhu, Y. Dong, Application of ceramic microfiltration membrane modified by nano-TiO2 coating in separation of a stable oil-in-water emulsion, J. Membr. Sci. 456 (2014) 128–133.

[58] J.-e. Zhou, Q. Chang, Y. Wang, J. Wang, G. Meng, Separation of stable oil–water emulsion by the hydrophilic nano-sized ZrO2 modified Al2O3 microfiltration membrane, Separ. Purif. Technol. 75 (2010) 243–248.